Strain-Driven Electric Field Control of Magnetization in FeGa/PMN-PT

Advanced Electronic Materials

ADVANCED ELECTRONIC MATERIALS Open Access

www.advelectronicmat.de

RESEARCH ARTICLE OPEN ACCESS

Strain-Driven Electric Field Control of Magnetization in FeGa/PMN-PT

Gajanan Pradhan[1] | Federica Celegato[1] | Alessandro Magni[1] | Deepak Dagur[2] | Marco Coisson[1] | Gabriele Barrera[1] | Paola Rizzi[3] | Piero Torelli[2] | Giovanni Vinai[2] | Paola Tiberto[1]

[1]Advanced materials and Life science Divisions, Istituto Nazionale di Ricerca Metrologica (INRIM), Torino, Italy | [2]CNR - Istituto Officina dei Materiali (IOM) Area Science Park, Trieste, Italy | [3]Chemistry Department and NIS, University of Turin (UNITO), Torino, Italy

Correspondence: Gajanan Pradhan (g.pradhan@inrim.it) | Paola Tiberto (p.tiberto@inrim.it)

Received: 15 August 2025 | **Revised:** 30 October 2025 | **Accepted:** 10 November 2025

Keywords: magnetic domains | magnetoelectric coupling | strain | X-ray magnetic circular dichroism

Abstract

Magnetoelectric materials are one of the potential candidates that can counter the growing need of low-power memory and spintronic devices due to their ability to electrically control magnetic states. Manipulation of a magnetic state with the sole use of an electric field has faced several challenges like volatility and non-reproducibility. Here, we propose a magnetostrictive FeGa thin film interfaced with a relaxor ferroelectric substrate (PMN-PT) having a [011] surface cut. The polarization rotation is controlled near the coercive electric fields and stabilized at remanence, which generates distinct strained states. This strain transfers to the FeGa layer mechanically, inducing a net rotation of magnetization without the need of any bias magnetic field applicators. Imaging of the magnetic domains reveals spatial and real-time information about its variation and adds insight on the modification of magnetic anisotropy. The newly created magnetic information can be erased by reaching ferroelectric saturation and subsequently regenerated through specific electrical pulses. These results demonstrate the possibility of manipulating the magnetization via controlled polarization rotation, for use in strain-driven magneto-electronics.

1 | Introduction

A new era in the search of energy efficient devices has emerged to tackle the growing requirements of current generation magnetic memory devices and sensors [1–6]. The significant increase in power consumption required for data storage and computing demands urgent attention for the development of novel materials or techniques that can be integrated with the current generation devices [7–12]. Magnetoelectric materials are well suited for these technological applications as the combination of ferromagnetic (FM) and ferroelectric (FE) material opens a wide opportunity for thorough investigation [13–22]. Manipulation of magnetism with electric fields has been researched in the past decade in both bulk single-phase multiferroic and artificial multiferroic materials. Even though the single-phase materials represent intrinsic FM and FE behavior, they are limited by low ordering temperatures [23, 24]. On the other side, artificial stacking of a FM layer with a FE material, sharing an interface, creates various possibilities of magnetoelectric coupling mechanisms like charge-mediated [25, 26], strain-mediated [27, 28], ion migration [29–31] etc. The magnetoelectric coupling coefficient of these heterostructures also becomes significantly larger than bulk ones [28, 32]. While each of these mechanisms have some advantages, strain-mediated magnetoelectric coupling is highly promising due to its non-volatile, reversible and robust nature as compared to others [33–36].

Electric field driven strain effects create a wide room for choosing different FM that can interface well with a FE material. A highly magnetostrictive FM material coupled with a high piezoelectric

coefficient material can be a promising candidate for enhanced effects due to its ability to show more variation in the magnetic properties under strain. Several works on FMs like Fe [37], Co [38], Ni [39, 40], CoFeB [41], FePt [42], FeCoSiB [43], or FeGa [44, 45] have been reported in literature showing changes in magnetic characteristics when associated with a piezoelectric via converse magnetostriction effect (CME). Another important parameter is the magnetic softness of the interfacial FM, which can allow the strain-induced anisotropy to be comparable with the magnetocrystalline anisotropy, allowing controlled magnetization rotation. Similarly, piezoelectric materials like $BaTiO_3$, $Pb[Zr_xTi_{1-x}]O_3$ (PZT), or $Pb(Mg_{1/3}Nb_{2/3})O_3$-$PbTiO_3$(PMN-PT) have been used in combination with a FM, showing reliable strain generation and cyclability [11, 46–48]. Relaxor ferroelectric PMN-PT, exhibiting a piezoelectric coefficient (d_{33}) in the range of 1500–2600 pC/N, has been extensively studied for its high CME. The out-of-plane polarization switching in PMN-PT under a bipolar electric field happens via fixed rotations passing through the metastable in-plane orientations. The polarization rotations of 71° and 180° result in a symmetric butterfly-like strain response with the electric field in the case of PMN-PT (001) crystallographic orientation [49, 50]. However, in PMN-PT(011), anisotropic strain behavior is observed due to the presence of 109° rotations (loop-like strain) [51]. When the PT concentration is 30%, the crystal structure is rhombohedral and the spontaneous polarization lies along the eight possible < 111 > orientations [52]. Under very high electric fields, orthorhombic crystal structure with polarization along the direction of electric field can also be generated [39].

Magnetization rotation has been reported to be around 90° when the polarization switches from positive to negative out-of plane orientation [53, 54]. In some reports, the angle is less than 90° due to the formation of sheer-strain and other effects compiling from pseudocubic axes of the piezoelectric [36]. These changes in magnetization are sufficient to generate variable magnetoresistive states for incorporation in magnetic tunnel junctions (MTJs) [10, 11]. The strain generated in a PMN-PT single crystal depends on intrinsic parameters like the %PT concentration, fabrication type and growth temperatures that decides the crystal structure. The initial strain generation under an electric field experiences some fatigue and requires a minimum of 4–5 cycles to stabilize the polarization switching paths [51]. In this perspective, the prime advantage of a PMN-PT(011) crystal is the stabilization of unique strain values at remanence (switching of fields) due to its asymmetric strain behavior. The ability to stabilize different remanent strained states can provide excellent control over generating unique magnetic properties.

In this work, we report a controlled rotation of the magnetic easy axis of FeGa film deposited on a PMN-PT(011) substrate by cycling a bipolar electric field applied across the thickness. FeGa was chosen due to its high magnetostriction, high tensile strength and soft magnetic behavior that makes it susceptible to small changes in strain [55–58]. The polarization of PMN-PT was controlled near to the coercive electric fields to stabilize different strained states. The samples were demagnetized, and the magnetic domains were recorded using MOKE to successfully visualize the anisotropy character and reorientation. The in-plane rotation of magnetization is correlated with the increase or decrease of interfacial strain, as measured by vibrating sample magnetometer (VSM) and x-ray magnetic circular dichroism (XMCD). Moreover, in-plane magnetic hysteresis curves were recorded to calculate the angle of easy axis rotation. A comparison of magnetic domains stabilized at different electric fields has been shown, which emphasizes the ability of FeGa film to perturb according to the strain magnitude. A reversible and non-volatile control on the magnetic properties has been achieved solely with the use of electric fields.

2 | Results and Discussion

2.1 | Magnetic and Electric Properties

The schematic of a magnetic FeGa thin film deposited on a unpolarized pristine PMN-PT(011) substrate is shown in Figure 1a. The FeGa layer has a mixed phase of ordered and disordered crystal structures as reported before in our work [56]. The top and bottom surfaces are connected to a voltage source that creates an out-of-plane electric field along the [011] direction. Before the application of any electric field to the piezoelectric, the magnetic hysteresis loops along different in-plane directions were measured using MOKE to determine the presence of any magnetic anisotropy. Figure 1b represents the magnetic hysteresis along [100], [01$\bar{1}$] and 45° with respect to [100]. The hysteresis along [01$\bar{1}$] has the highest remanence, depicting a sharp magnetization reversal as compared to the other directions, where a lower remanence is reported. The difference in hysteresis along the three directions marks the presence of a magnetic anisotropy in the pristine state with a possible easy axis (EA) along [01$\bar{1}$]. Figure 1c shows a rhombohedral phase structure of the PMN-PT crystal owing to its [011] cut. The out-of-plane polarization can be defined by [$\bar{1}$11] or [111] components (orange arrows) during positive saturation and by [1$\bar{1}\bar{1}$] or [$\bar{1}\bar{1}\bar{1}$] components (purple arrows) during negative saturation. The switching of polarization from positive to negative is mediated through four in-plane variants along [11$\bar{1}$], [1$\bar{1}$1], [$\bar{1}\bar{1}$1] and [$\bar{1}$1$\bar{1}$] orientations as marked by the blue arrows. The sample surface and the edges, ([01$\bar{1}$] and [100]) are represented by the blue plane and the black arrows. An application of a bipolar electric field cycled across the thickness of the PMN-PT modifies the net polarization of the material that is usually depicted by the polarization hysteresis (P-E curve). We have measured the current generated in the circuit while cycling the field with a maximum magnitude of 6 kV/cm. The current vs electric field ($I(E)$) curve obtained (Figure 1d) marks two distinct characteristic peaks near to $E \approx 1.8$ kV/cm. The peaks correspond to the two coercive electric fields ($\pm E_c$) where the polarization vectors switch from out-of-plane to in-plane variants. This increasing current is associated with the domain switching phenomena of the piezoelectric material [59].

2.2 | Strain History and Stabilization

The application of an electric field across the opposite surfaces of a piezoelectric, alters its dimensions due to the inverse piezoelectric effect. The in-plane strains generated are measured using a biaxial strain gauge that is adhered to the sample surface. The dependence of strains generated along [01$\bar{1}$] and [100] directions on the cycling electric field is shown by the green and red curves, respectively, in Figure 2a. The amplitude

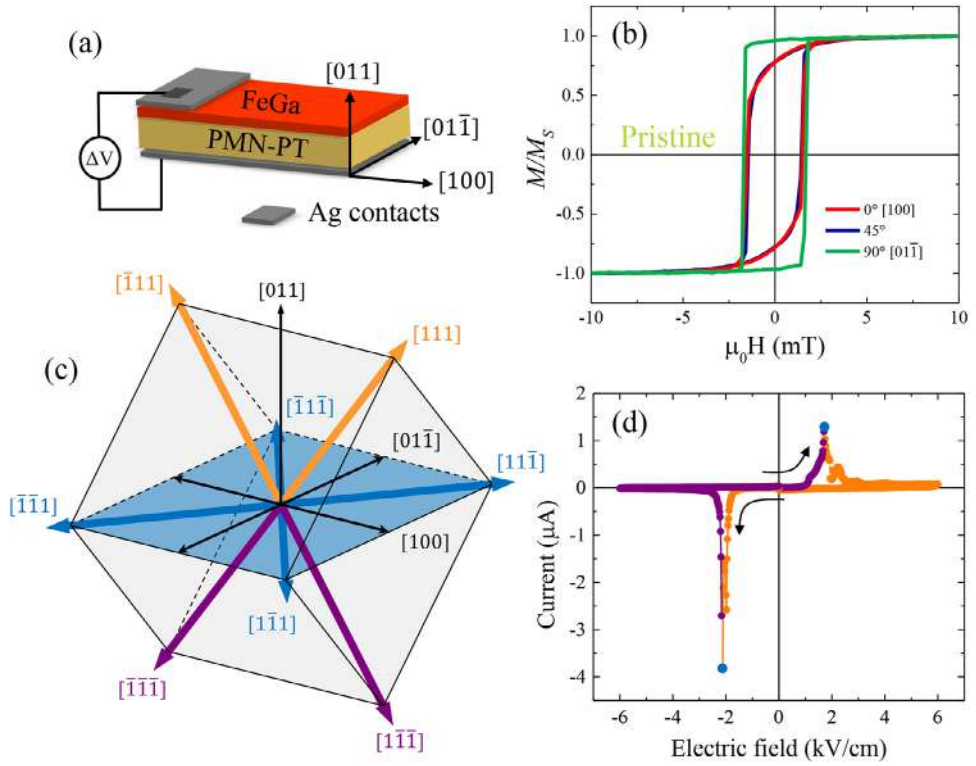

FIGURE 1 | (a) Schematic of FeGa thin film on PMN-PT(011) crystal substrate with Ag contacts as top and bottom electrodes for application of electric field (not to scale). (b) Evolution of magnetic hysteresis along in-plane axes (0°, 45°, 90° from [100]) in the pristine state (before application of electric field). (c) Rhombohedral unit cell showing the crystal axes shown in (a) and the 8 possible polarization orientations in PMN-PT(011). (d) Current vs electric field ($I(E)$ curve) of PMN-PT(011) showing the characteristic peaks which marks the coercive field (E_c) values where polarization switching occur. The different colors in the $I(E)$ curve correspond to the different polarization configurations shown in (c).

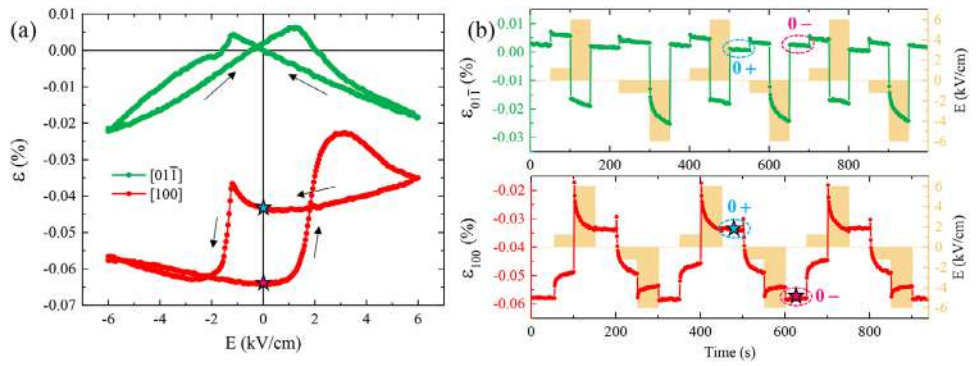

FIGURE 2 | (a) In-plane strain generated along [01$\bar{1}$] and [100] directions with cycling electric field of amplitude between ±6 kV/cm are represented by the green and red curve. (b) The strain evolution under continuous application of ±6 and near ±1.2 kV/cm are shown marking the stability at 0+ and 0− states. The portions of electric field application are marked with light yellow color.

of the field is cycled between ± 6 kV/cm from the pristine state until a repeatable strain curve is achieved. The initial electric field application creates a polarization switching path by reorienting the crystal axes. After repeated polarity reversing, the polarization path saturates gradually, thus generating a repeatable strain curve. The approach of the strain curve to and from +6 kV/cm are significantly different along [100]. This indicates that the saturation polarization is not achieved during positive electric field application. A saturating behavior, however, would represent a further decreasing magnitude of strain (for $E > E_c$) stabilizing at values similar to negative cycles [51]. The switching of polarization in the PMN-PT crystal takes place via 109° or 71°/180° rotations. The former is responsible for generating a loop-like strain behavior as a function of bipolar electric field, while the latter is responsible for a butterfly-like strain dependence. In the case of PMN-PT(011) crystal cut, a combination of both rotations can create a net asymmetry in the strain hysteresis as observed previously observed in similar systems [49, 50].

The strain curve has an asymmetric dependence as compared to our earlier report on PMN-PT(001) crystal, where it is symmetric

[45]. This behavior stabilizes two different remanent strained states depending on the poling direction. Along the 01$\bar{1}$ direction, two strain peaks are observed near to E_c at values of approximately ± 1.2 kV/cm, which marks the in-plane polarization states. The presence of strain peaks at sub-coercive field values can be attributed to the influence of non-180° ferroelastic domain switching that have been observed to affect the strain values [60]. The presence of the PMN-30%PT substrate near to the morphotropic phase boundary can induce such effects. As the saturation fields are approached, the strain decreases as the out-of plane polarization rotation stretches the PMN-PT along [011] direction. The strains generated along both in-plane directions are measured as a function of time to understand its stability at various levels. A constant DC electric field of ±6 and ±1.2 kV/cm was applied alternatively via the zero field (remanence) states. The variation of strain levels is shown in Figure 2b by green [01$\bar{1}$] and red [100] curves, and the corresponding levels of voltage activation are marked by light yellow patches.

The evolution of strain under constant electric fields provides insight about the stability of a particular strained state. Under $E = -6$ kV/cm, ε_{100} becomes stable after 50 s at around –0.054% while the $\varepsilon_{01\bar{1}}$ is still decreasing. Similarly, at $E = +6$ kV/cm, $\varepsilon_{01\bar{1}}$ is nearly stable around −0.018% while ε_{100} is reducing. This suggest that the saturation is not achieved fully and the polarization reorientation in still undergoing. Indeed, a gradual decrease in behavior is observed for a time period of more than 1000 s, representing a slowly saturating behavior as shown in Figure S5 (Supporting Information). This is directly linked to the non-overlapping part of the curves near to ±6 kV/cm. Near to E_c, the $\varepsilon_{01\bar{1}}$ is stable around its peak values, whereas the ε_{100} is not since it experiences a large strain jump. Under a continuous application of $E \approx -E_c$, the strain along [100] goes up instantly, representing the peak in Figure 2a and drops down further representing the switching of polarization. Similar jump is observed after 0− state, which marks the instability of strain near to E_c. Overall, as the field is switched off, the strain along both the directions are stable and distinct. The remanent strained state achieved after a negative and positive field cycles are hereby named as **0−** and **0+** state, respectively represented by pink and blue symbols. The two remanent strained states are shown to stabilize a greater difference in strain values along [100] direction of around 0.024% with a negligible change along [01$\bar{1}$].

2.3 | Controlling Magnetic Domains

The in-plane strain generated at the interface between FeGa and PMN-PT is transferred to the magnetic layer via the inverse magnetostriction effect. This affects the magnetic anisotropy of the system, thereby modifying the magnetic domain structure. In order to have a deeper understanding of this effect, magnetic domains were recorded under a MOKE microscope. A 20× magnification objective was used to capture a wide domain area of 300 × 300 μm^2. The sample was magnetically demagnetized by applying an alternating in-plane magnetic field (H_{peak} = 20 mT, frequency = 13 Hz, decay time = 2 s) along the pristine HA at different polarized states. The Kerr contrasts were recorded in the same region as shown in Figure 3. A simultaneous acquisition of longitudinal (along [100]) and transverse (along [01$\bar{1}$]) components (in-plane contrasts) was performed to determine the preferential orientation of domains. The images on left of each state represent the **L** contrast (**M** ∥ **H**) and on the right are the **T** contrast (**M** ⊥ **H**). Demagnetization under a decaying alternating magnetic field lowers the magnetic energy of FeGa letting the domains to point along the easy axis of the system. The domain patterns are statistically repeatable until a fixed frequency of AC field is kept. Here, we consider the 0− state (Figure 3b) as the reference, in which the strain is the most compressive along [100]. The components of magnetization are majorly along the **T** direction representing stripe domain pattern. The faint **L** contrasts represents very minimal component of magnetization along [100]. The relative change in % strain of each states (compared to 0− state) are calculated as the strain changes along both directions are asymmetric. Since [01$\bar{1}$] is the pristine EA of the system, any expansion along it would reinforce the original EA while any contraction would rotate domains toward [100]. Further, any expansion along [100] would rotate the EA toward [100]. A compression of −0.024% along [01$\bar{1}$] under −6 kV/cm rotates some of the domains toward [100] as marked by the yellow regions in Figure 3a. The direction of magnetic domains are referenced by the red arrows. The domains at E field value of +1.2 kV/cm are similar to those of the 0− state (Figure 3c). Once the E_c is crossed and the field has reached to +6 kV/cm, a compression along [01$\bar{1}$] and expansion along [100] is observed as shown in Figure 3d. This hugely impacts the domain structure stabilization showing a significant increase in longitudinal domains (marked by the yellow circles with red arrows). Some regions still show the stripe patterns along [01$\bar{1}$], similarly to the 0− state marked by the green enclosures. As the field is zeroed to achieve the 0+ state, a similar magnetic configuration is retained after demagnetization as shown in Figure 3e. This is directly linked to the non-saturating behavior of the piezoelectric polarization that generates a minor strain curve and produces a different remanent strain. Moreover, the area of stripe domains has increased in the 0+ state since the compression along [01$\bar{1}$] has reversed whilst maintaining the expansion along [100]. This magnetic behavior is retained (Figure 3f) until the polarization is reversed by approaching −6 kV/cm.

The region corresponding to the domain observation represents a smaller area of 0.09 mm^2, whereas the strain curves shown in Figure 2 represent the macroscopic behavior averaged on the whole surface, with an area of nearly 20 mm^2. This larger surface includes regions with different local strains that contributes to generate a net strain [61]. The strain inhomogeneity can be occurring due to the underlying presence of complex piezoelectric domains of PMN-PT that forms during the electric field switching [62]. This disorderliness has a direct implication on the local magnetic anisotropies as the FeGa film is deformed in a non-uniform manner, thus stabilizing different domains in different regions. Indeed, the non-uniformity in domain patterns is clearly observed in Figure 3 after the polarization of the PMN-PT. The magnetic domains near to E_c remains similar to the 0+ or 0− states, until a strain jump (polarization switching) occurs. The exact quantification of domain changes cannot be linked to the strain-time curves in Figure 2 due to limited area MOKE measurement. Further, the strained states near to E_c can also be impacted by the rate at which a particular electric field is approached. A linear increase compared to a sudden jump in the electric field sometimes affects the patterning of domains.

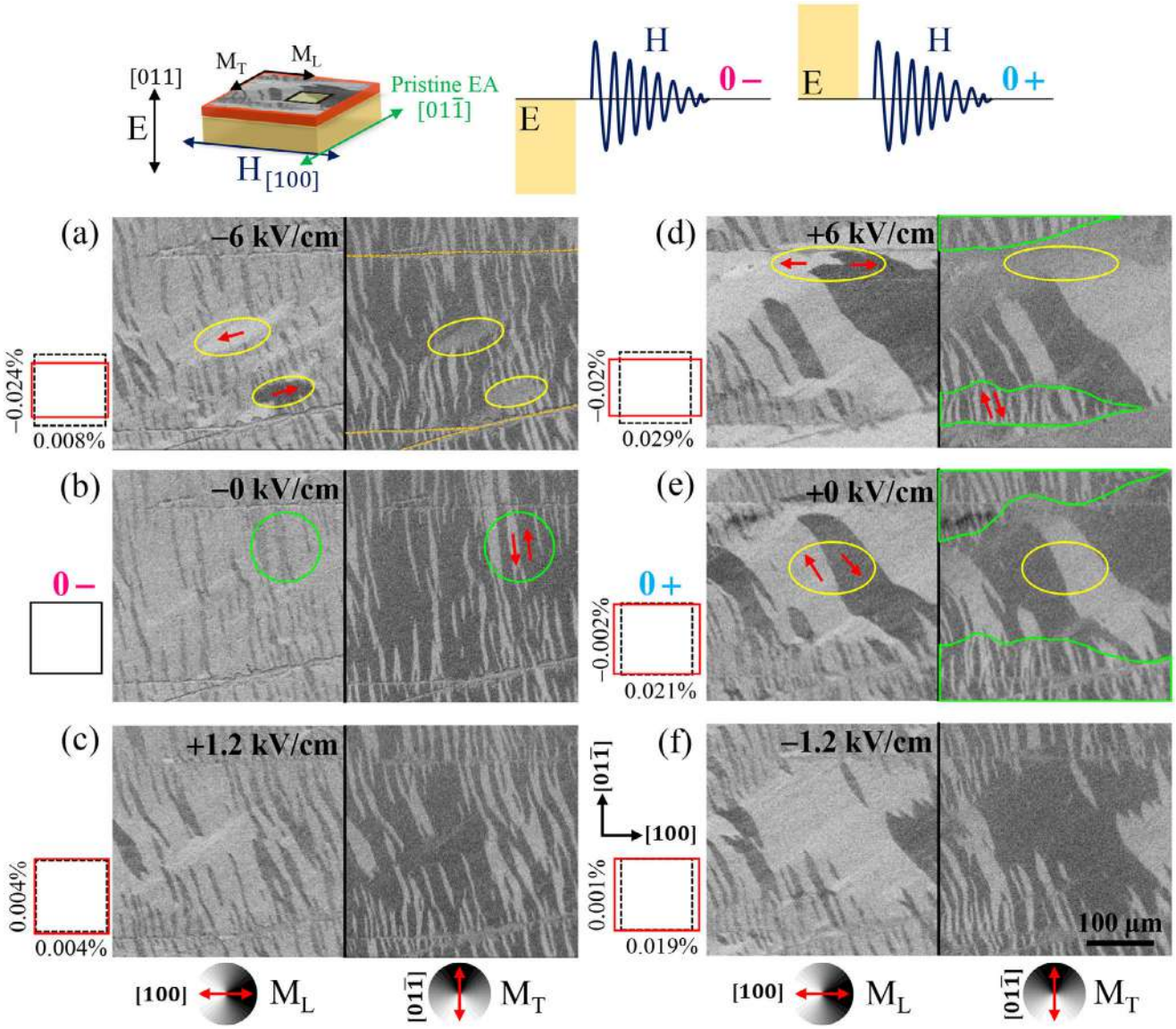

FIGURE 3 | Schematic of measurement procedure using MOKE to obtain the demagnetized states at various strained states. A small area of the sample is observed under the microscope as marked. (a–f) Magnetic domain contrasts of demagnetized states recorded at six distinct strained states achieved under applied electric fields of ±6, ±0 and ±1.2 kV/cm. For each state, the left and the right images represent the longitudinal (in-plane **M** ∥ **H**) and transverse (in-plane **M** ⊥ **H**) MOKE contrasts. The relative change of strain (%) with respect to 0− state (b) generated along both [100] and [01$\bar{1}$] are shown on the left.

2.4 | Rotation of Magnetic Anisotropy

2.4.1 | Magnetization Reversal

The magnetic domain textures forming during the magnetization reversal along [100] and [01$\bar{1}$] directions are further studied to understand the influence of electric-field induced local strains. In the pristine state, large domains are observed along [01$\bar{1}$] while magnetic ripple patterns are observed along the [100] as shown in Figure S6 (Supporting Information). This is typical along the hard axis of soft polycrystalline thin films such as FeGa films. Once switched in 0− and 0+ states, the domain textures and shapes changes. Figure 4a,b show the same region after switching the electric polarization to 0− and 0+, respectively. The local hysteresis loops shown on the left, refers to the specified domain area. For the 0− state (Figure 4b), faint domains are observed along [100] (HA) where the reversal majorly happens via coherent rotation along with some ripple patterns. The annihilation of these ripples marks the influence of local substrate strains caused by the ferroelectric domains underneath. Along the easy axis ([01$\bar{1}$]), a clear 180° domain wall was observed similarly to the original easy axis of the sample. The loops corresponding to the transverse contrast change for the 0+ state and 0− state are shown in Figure S7 (Supporting Information). Some surface cracks also form after repeated switching of the piezoelectric polarization as marked by the dashed orange lines, in agreement with what was reported in literature [37]. The morphology of these cracks are shown in Figure S8 (Supporting Information). In the 0+ state, the domain structures along [100] and [01$\bar{1}$] are smaller. The pinning of domains can be referred to the surface morphological character (marked by the dashed yellow lines) also shown in Figure S8 (Supporting Information). It is interesting to note that

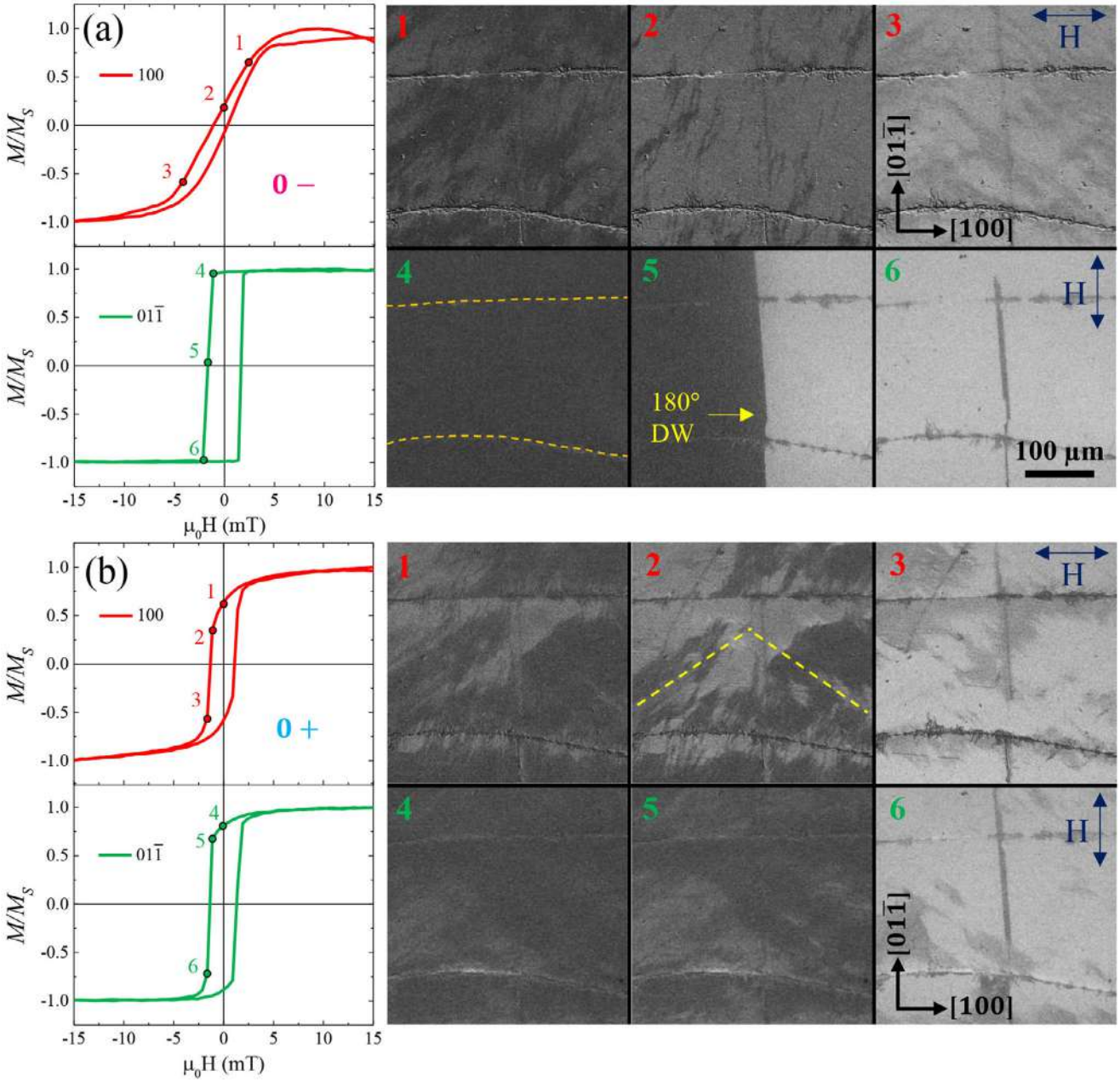

FIGURE 4 | Magnetic domain structures recorded during magnetization reversal in 0− and 0+ states are shown by (a) 1–6 and (b) 1–6, respectively. The orange dotted lines mark the surface cracks generated by electric-field induced strain. The red and green curves represent the local hysteresis loop (corresponding to area shown) along [100] and [01$\bar{1}$] directions. The images correspond to the points marked in the hysteresis loops.

the domains along the [100] direction are now bigger as compared to those of the 0− state, suggesting the shift of EA toward [100]. Along the [01$\bar{1}$], the previously easy axis (0− state) is modified toward a mix contribution of surface induced magnetization rotation and domain wall motion.

2.4.2 | Hysteresis Evolution

The macroscopic magnetic hysteresis loops along different in-plane directions were measured using MOKE to determine its evolution under positive and negative electric field bias. The beam diameter was ~1 mm to generate a net average contribution. Figure 5a,b show the evolution of magnetic hysteresis in 0− and 0+ states, respectively. In the 0− state, the hysteresis loops along 90° [01$\bar{1}$] have the highest remanence. As the θ (angle from [100]) reduces, the remanent magnetization decreases and becomes the lowest at 0°. In the 0+ state, the loops are modified due to a different underlying strain with the hysteresis along [100] having higher remanence than [01$\bar{1}$]. The polar plot of normalized magnetic remanence (M_r/M_s) of hysteresis measured in different directions and states is shown Figure 5c. The pristine state curve, shown by light green color has an easy axis along the [01$\bar{1}$] direction. The anisotropy is modified in the 0+ state, represented by the blue curve. The remanence of hysteresis along 90° and −90° are not the same as the sample generates cracks and local surface deformations that hinders the symmetry of the domain flow [61, 63]. In the 0− state, the shape of

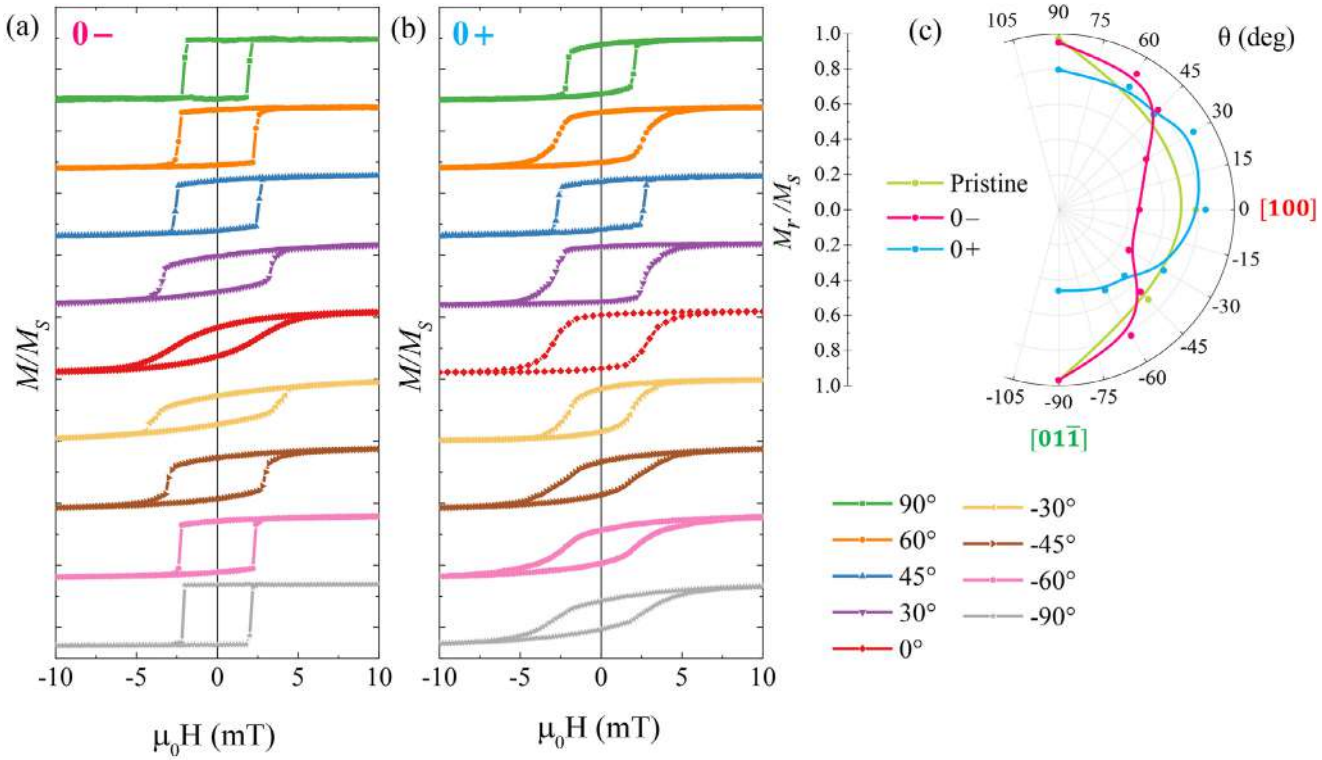

FIGURE 5 | Evolution of magnetic hysteresis along different in-plane axes (across an angle of 180°) in the 0− and 0+ states are shown in (a) and (b), respectively. (c) Polar plot of magnetic remanence vs. measured angle with respect to [100] direction.

the polar plot completely shifts, making the [01$\bar{1}$] direction as the easy axis of the 0− state. Overall, a more pronounced magnetic anisotropy is observed in the 0− state as compared to the 0+ state. The anisotropy change observed via the shift of hysteresis loops can be quantitatively compared with the expected change due to the stress-induced magnetoelastic contribution. The details of the in-plane anisotropy change are discussed in Supporting Information.

2.5 | Magnetization Dependence on Remanent Strain

The influence of induced strain on the magnetization of FeGa was measured in absence of any external magnetic field. A schematic representation of the 0− and 0+ states is shown in Figure 6a with the relative strain values depicting expansion along [100] and slight compression along [01$\bar{1}$]. The sample was characterized by XMCD measurements at Fe $L_{2,3}$-edge. The XMCD signals show an immediate reduction of dichroic signal at remanence on the first application of electric field induction across the PMN-PT substrate as shown in Figure S9 (Supporting Information). The magnetic moment is recorded simultaneously along the [01$\bar{1}$] and [100] directions using a VSM to determine the rotation of magnetic moments. Figure 6b,c show the variation of magnetic moments along [100] and along [01$\bar{1}$] as a function of time under repeated electric field pulses. After each pulse, the magnetic moment is averaged for 30 s and are represented by the pink and blue squares for the 0− and 0+ states, respectively. Along the [100] direction, the magnetic moment increases as the 0− state is switched to 0+. This correlates well with the expansion along [100] that forces the net magnetic moment to turn toward it. Under similar circumstances, a decrease in moment is observed along the [01$\bar{1}$] representing a rotation of magnetization. This shifts the magnetic EA from [01$\bar{1}$] in 0− state toward the direction of [100] in 0+ state. The negative or positive pulse are repeated for 10 cycles each to maximize the effect of magnetic reorientation. During the transition from −6 to +6 kV/cm pulse, we observe an initial jump of magnetic moment that slowly saturates after at least 4 repeated pulses. This is related to the fatigue that occurs in PMN-PT during polarization switching, which subsequently affects the strain transfer efficiency.

3 | Conclusion

The magnetic properties of a FeGa film have been modified by sole use of electric fields. The application of an electric field generates strain at the interface that is inhomogeneous in nature and depends on the crystallographic changes to PMN-PT during polarization reorientation. This creates a unique but complex dependence of magnetic anisotropy and domains on strain. Combining mechanic, electric and magnetic characterizations, we experimentally prove the full electric control of FeGa thin films by modifying the piezoelectric (control layer) using an electric field. Majorly, different strain levels are achieved in a reproducibly controlled manner, thereby tuning the magnetic responses. Different anisotropy levels in FeGa are shown to be stabilized at zero electric fields after a positive/negative pulse. The rotation of in-plane magnetization in remanent strained states (0− and 0+ states) is proved by combining the VSM and XMCD measurements. A change in easy axis between these

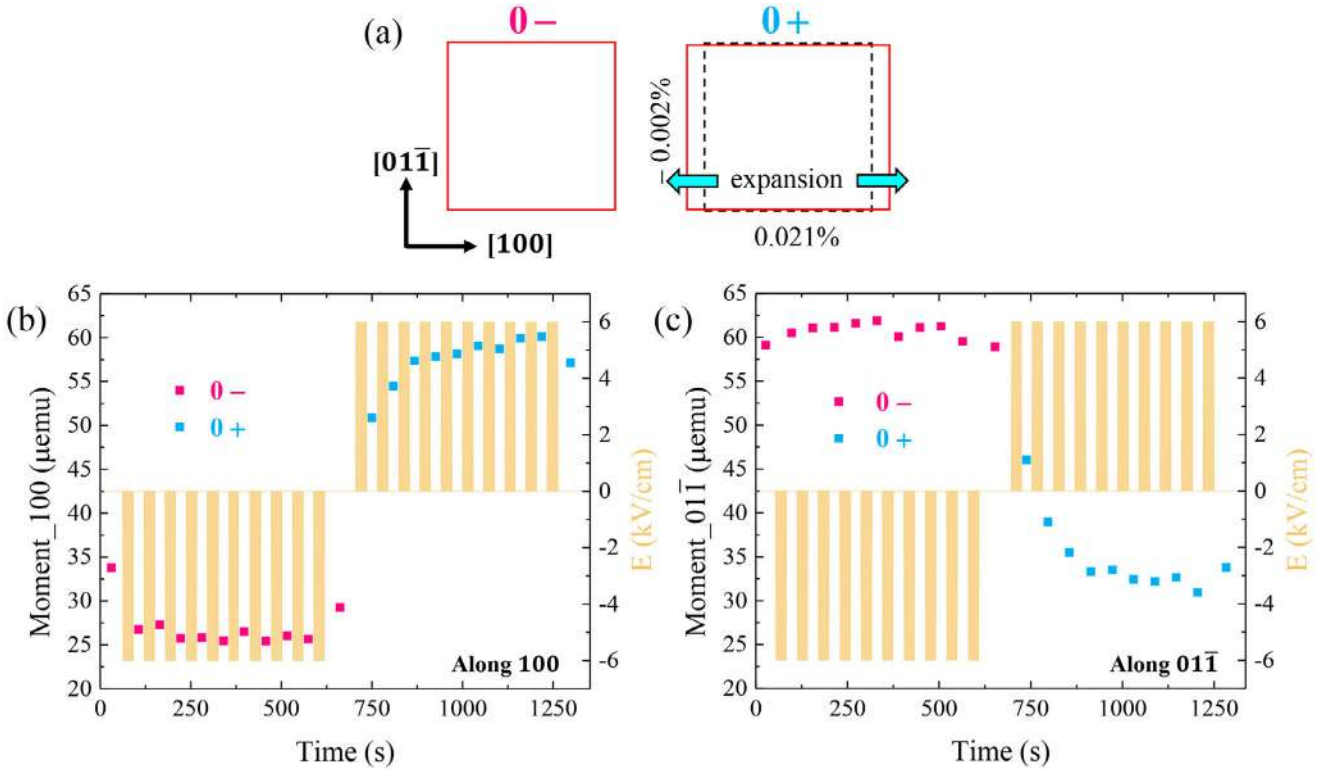

FIGURE 6 | (a) Schematic of relative expansion and contraction at 0+ state with respect to 0− state. (b,c) Magnetization recorded using VSM along [01$\bar{1}$] and [100] directions after repeated application of electric field pulses of ±6 kV/cm. The pink and light blue points mark the average magnetization after each pulse recorded both along [100] and [01$\bar{1}$] demonstrating a rotation of magnetic moments.

states is also presented, as studying the demagnetized states reveals an increase in longitudinal contrast. This can only be attributed to the inclusion of strain-induced anisotropy in the system. The anisotropy variation was further analyzed by the change in magnetic hysteresis along different in-plane axes. The magnetic domains recorded during the magnetization reversal reveals the effect of net anisotropy rotation and local surface modifications on the magnetic character. This work proves that the effect of strain-mediated magnetoelectric coupling can be significant when a proper control of the piezoelectric polarization is achieved. The FeGa/PMN-PT artificial multiferroic heterostructure possess huge potential to be incorporated in low power magneto-electronics.

4 | Experimental Section

4.1 | Sample Preparation

Radio frequency (RF) sputtering technique was used to deposit FeGa thin films on (011) oriented PMN-30%PT substrates. The target used for deposition has a composition of 70:30 (Fe:Ga). The deposition rate of FeGa was maintained at 0.8 Å/s and the thickness of FeGa layer was chosen to be 20 nm. The PMN-PT substrates were bought from Crystal Gmbh, Germany having a thickness of 0.5 mm. The substrates were used in their pristine condition and any annealing treatments were not performed to avoid thermal effects [64]. The deposition was performed on the polished side of the substrate at room temperature and in Ar ion environment at a pressure of 1.1×10^{-2} mbar. The base pressure of the chamber was 10^{-7} mbar. No external magnetic field was applied during the deposition. Scanning electron microscope (SEM by FEI Quanta3D-Inspect F) was used to determine the growth quality. The elemental configuration and morphology of the FeGa film measured by X-ray photoelectron spectroscopy (XPS) and SEM are shown in Figures S1 and S2, respectively (Supporting Information). The surface roughness of < 1 nm was observed for the PMN-PT substrate using atomic force microscope (AFM) which ensures a uniform FeGa layer. Energy dispersive X-ray spectroscopy (EDS) maps represent a compositional homogeneity of Fe and Ga atoms present in the sample (Figure S3 (Supporting Information)). The composition of deposited FeGa thin film is 68.71:21.29 (Fe:Ga) as recorded from the EDS spectra shown in Figure S4 (Supporting Information).

4.2 | Electric-Field Induced Strain Application

Silver (Ag) paste was used as the bottom electrode of PMN-PT with FeGa layer as the top electrode as shown in Figure 1a. These electrodes were connected to the voltage source of a Keithley 6517A Electrometer for generating an electric field across the sample. The strain generated in the PMN-PT was measured using a biaxial strain gauge that is attached to the sample surface. The internal resistance and the k-factor of the strain gauge were 120 Ohms and 1.67, respectively. The measuring strain gauge was attached via a half-wheatstone bridge setup to a reference gauge of the same specifications. Any change in the resistance caused by the expansion or contraction of the measuring strain gauge was measured using a HBM MGCplus data acquisition

system. The strain value is calibrated for a fixed resistance and is measured in ppm. $I(E)$ curves were recorded using a Keithley 6485 picoammeter/voltage source by measuring the current flow through the thickness of the sample under a cycling electric field within ±6 kV/cm.

4.3 | Magnetic Domains and Hysteresis

The magnetization of the sample was recorded using VSM, by Lakeshore Cryotronics, Inc in absence of magnetic field. The in-plane magnetization components (along $[01\bar{1}]$ and [100]) were measured simultaneously using two separate pick-up coils. The magnetic hysteresis loops along different in-plane angles were measured using longitudinal magneto-optic Kerr effect (MOKE). A s-polarized laser with a wavelength of 658 nm and 8mW power was used [65]. To image the magnetic domains, another MOKE setup equipped with a microscope by Evico magnetics was used. A magnification of 20× was considered for optimal viewing of domains. The demagnetized states were recorded with a simultaneous acquisition of longitudinal (**L**) and transverse (**T**) contrasts at different electric fields applied to the PMN-PT. The magnetic hysteresis along with domains at each step of the magnetization reversal were recorded in longitudinal mode. All measurements are performed at room temperature.

4.4 | X-ray Magnetic Circular Dichroism

XMCD spectra at Fe $L_{2,3}$ edges were measured in the APE-HE beamline at Elettra synchrotron facility in Trieste [66]. A custom designed sample holder was used for in situ voltage application. The spectra were measured in total electron yield (TEY) mode in circular polarization, with a normalizing the intensity of the sample current to the incident photon flux current. For each energy value, a magnetic field pulse of ±20 mT was applied in plane (a field large enough to switch and saturate the magnetization of the sample), measuring the TEY signal at remanence. The sample surface was kept at 45° with respect to the incident X-rays for a beam footprint of around 200 μm width.

Acknowledgements

This work has received funding from the European Union's Horizon 2020 research and innovation programme under the Marie Skłodowska–Curie grant agreement No 861145. The experimental work has been partially performed at NanoFacility Piemonte, an INRIM laboratory supported by Compagnia di San Paolo. XMCD and XPS characterizations were performed in the framework of the Nanoscience Foundry and Fine Analysis (NFFA-MUR Italy Progetti Internazionali) facility (https://www.trieste.nffa.eu/).

Conflicts of Interest

The authors declare no conflicts of interest.

Data Availability Statement

The data that support the findings of this study are available from the corresponding author upon reasonable request.

References

1. S. Wolf, D. Awschalom, R. Buhrman, et al., "Spintronics: A Spin-Based Electronics Vision for the Future," *Science* 294, no. 5546 (2001): 1488–1495.

2. J. Åkerman, "Toward a Universal Memory," *science* 308, no. 5721 (2005): 508–510.

3. M. Bibes and A. Barthélémy, "Towards a Magnetoelectric Memory," *Nature Materials* 7, no. 6 (2008): 425–426.

4. J. Scott, "Multiferroic Memories," *Nature Materials* 6, no. 4 (2007): 256–257.

5. C. M. Leung, J. Li, D. Viehland, and X. Zhuang, "A Review on Applications of Magnetoelectric Composites: From Heterostructural Uncooled Magnetic Sensors, Energy Harvesters to Highly Efficient Power Converters," *Journal of Physics D: Applied Physics* 51, no. 26 (2018): 263002.

6. S. Bandyopadhyay, J. Atulasimha, and A. Barman, "Magnetic Straintronics: Manipulating the Magnetization of Magnetostrictive Nanomagnets with Strain for Energy-Efficient Applications," *Applied Physics Reviews* 8, no. 4 (2021).

7. S. Manipatruni, D. E. Nikonov, and I. A. Young, "Beyond Cmos Computing with Spin and Polarization," *Nature Physics* 14, no. 4 (2018): 338–343.

8. S. Manipatruni, D. E. Nikonov, C.-C. Lin, et al., "Scalable Energy-Efficient Magnetoelectric Spin–Orbit Logic," *Nature* 565, no. 7737 (2019): 35–42.

9. C. Chappert, A. Fert, and F. N. Van Dau, "The Emergence of Spin Electronics in Data Storage," *Nature Materials* 6, no. 11 (2007): 813–823.

10. A. Chen, Y. Wen, B. Fang, et al., "Giant Non-volatile Manipulation of Magnetoresistance in Magnetic Tunnel Tunctions by Electric Fields via Magnetoelectric Coupling," *Nature Communications* 10, no. 1 (2019): 243.

11. Y. Zhang, W. Sun, K. Cao, et al., "Electric-Field Control of Non-volatile Resistance State of Perpendicular Magnetic Tunnel Junction via Magnetoelectric Coupling," *Science Advances* 10, no. 16 (2024): eadl4633.

12. A. Fert, R. Ramesh, V. Garcia, F. Casanova, and M. Bibes, "Electrical Control of Magnetism by Electric Field and Current-Induced Torques," *Reviews of Modern Physics* 96, no. 1 (2024): 015005.

13. R. Ramesh and N. A. Spaldin, "Multiferroics: Progress and Prospects in Thin Films," *Nature Materials* 6, no. 1 (2007): 21–29.

14. W. Eerenstein, N. Mathur, and J. F. Scott, "Multiferroic and Magnetoelectric Materials," *nature* 442, no. 7104 (2006): 759–765.

15. S.-W. Cheong and M. Mostovoy, "Multiferroics: a Magnetic Twist for Ferroelectricity," *Nature Materials* 6, no. 1 (2007): 13–20.

16. N. A. Spaldin and R. Ramesh, "Advances in Magnetoelectric Multiferroics," *Nature Materials* 18, no. 3 (2019): 203–212.

17. J.-M. Hu, L.-Q. Chen, and C.-W. Nan, "Multiferroic Heterostructures Integrating Ferroelectric and Magnetic Materials," *Advanced Materials* 28, no. 1 (2016): 15–39.

18. F. Matsukura, Y. Tokura, and H. Ohno, "Control of Magnetism by Electric Fields," *Nature Nanotechnology* 10, no. 3 (2015): 209–220.

19. C. Li, A. Tang, Y. Cheng, et al., "Full Perpendicular Switching of Ferrimagnetic Order by Electric-Field with Ultralow Assisting Magnetic Field," *Advanced Functional Materials* (2025): e13870.

20. T. Usami, Y. Sanada, S. Fujii, et al., "Artificial Control of Giant Converse Magnetoelectric Effect in Spintronic Multiferroic Heterostructure," *Advanced Science* 12, no. 7 (2025): 2413566.

21. F. Maccherozzi, M. Ghidini, M. Vickers, et al., "Inverted Shear-Strain Magnetoelastic Coupling at the Fe/Batio3 Interface from Polarised X-Ray Imaging," *Nature Communications* 16, no. 1 (2025): 8445.

22. D. Arora and D. Kaur, "Frequency Tunable Film Bulk Acoustic Resonator Integrating Pmn-Pt/Fsma Multiferroic Heterostructure for Flexible Mems," *Advanced Materials Technologies* 10, no. 7 (2025): 2400971.

23. N. A. Hill, "Why Are There so few Magnetic Ferroelectrics?", *The Journal of Physical Chemistry* 104, no. 29 (2000): 6694–6709.

24. J. F. Scott, "Room-Temperature Multiferroic Magnetoelectrics," *NPG Asia Materials* 5, no. 11 (2013): e72–e72.

25. A. Chernyshov, M. Overby, X. Liu, J. K. Furdyna, Y. Lyanda-Geller, and L. P. Rokhinson, "Evidence for Reversible Control of Magnetization in a Ferromagnetic Material by Means of Spin–Orbit Magnetic Field," *Nature Physics* 5, no. 9 (2009): 656–659.

26. T. Nan, Z. Zhou, M. Liu, et al., "Quantification of Strain and Charge Co-Mediated Magnetoelectric Coupling on Ultra-Thin Permalloy/Pmn-Pt Interface," *Scientific Reports* 4, no. 1 (2014): 3688.

27. C. Thiele, K. Dörr, O. Bilani, J. Rödel, and L. Schultz, "Influence of Strain on the Magnetization and Magnetoelectric Effect in La 0.7 a 0.3 Mn o 3/ Pmn- Pt (001)(a= sr, ca)," *Physical Review B* 75, no. 5 (2007): 054408.

28. W. Eerenstein, M. Wiora, J. Prieto, J. Scott, and N. Mathur, "Giant Sharp and Persistent Converse Magnetoelectric Effects in Multiferroic Epitaxial Heterostructures," *Nature Materials* 6, no. 5 (2007): 348–351.

29. M. Weisheit, S. FÃhler, A. Marty, Y. Souche, C. Poinsignon, and D. Givord, "Electric Field-Induced Modification of Magnetism in Thin-Film Ferromagnets," *Science* 315, no. 5810 (2007): 349–351.

30. U. Bauer, L. Yao, A. J. Tan, et al., "Magneto-Ionic Control of Interfacial Magnetism," *Nature Materials* 14, no. 2 (2015): 174–181.

31. J. Jeong, N. Aetukuri, T. Graf, T. D. Schladt, M. G. Samant, and S. S. Parkin, "Suppression of Metal-Insulator Transition in Vo2 by Electric Field–Induced Oxygen Vacancy Formation," *Science* 339, no. 6126 (2013): 1402–1405.

32. J. Heron, J. Bosse, Q. He, et al., "Deterministic Switching of Ferromagnetism at Room Temperature Using an Electric Field," *Nature* 516, no. 7531 (2014): 370–373.

33. R. Cherifi, V. Ivanovskaya, L. Phillips, et al., "Electric-Field Control of Magnetic Order Above Room Temperature," *Nature Materials* 13, no. 4 (2014): 345–351.

34. G. Radaelli, D. Petti, E. Plekhanov, et al., "Electric Control of Magnetism at the Fe/Batio3 Interface," *Nature Communications* 5, no. 1 (2014): 3404.

35. M. Ghidini, F. Maccherozzi, X. Moya, et al., "Perpendicular Local Magnetization Under Voltage Control in Ni Films on Ferroelectric Batio3 Substrates," *Advanced Materials* 27, no. 8 (2015): 1460–1465.

36. M. Ghidini, R. Mansell, F. Maccherozzi, et al., "Shear-Strain-Mediated Magnetoelectric Effects Revealed by Imaging," *Nature Materials* 18, no. 8 (2019): 840–845.

37. F. Motti, G. Vinai, V. Bonanni, et al., "Interplay between Morphology and Magnetoelectric Coupling in Fe/Pmn-Pt Multiferroic Heterostructures Studied by Microscopy Techniques," *Physical Review Materials* 4, no. 11 (2020): 114418.

38. N. D'Souza, M. Salehi Fashami, S. Bandyopadhyay, and J. Atulasimha, "Experimental Clocking of Nanomagnets with Strain for Ultralow Power Boolean Logic," *Nano Letters* 16, no. 2 (2016): 1069–1075.

39. S. Lindemann, J. Irwin, G.-Y. Kim, et al., "Low-Voltage Magnetoelectric Coupling in Membrane Heterostructures," *Science Advances* 7, no. 46 (2021): eabh2294.

40. D. Dagur, V. Polewczyk, A. Y. Petrov, et al., "Visible Light Effects on Photostrictive/Magnetostrictive Pmn-Pt/Ni Heterostructure," *Advanced Materials Interfaces* 9, no. 36 (2022): 2201337.

41. S. Zhang, Y. Zhao, P. Li, et al., "Electric-Field Control of Non-volatile Magnetization in co 40 Fe 40 B 20/Pb (Mg 1/3 Nb 2/3) 0.7 ti 0.3 o 3 Structure at Room Temperature," *Physical Review Letters* 108, no. 13 (2012): 137203.

42. L. Leiva, J. A. Torres, J. E. Gomez, D. V. Rodriguez, J. Milano, and A. Butera, "Electric Field Control of Magnetism in Fept/Pmn-Pt Heterostructures," *Journal of Magnetism and Magnetic Materials* 544 (2022): 168619.

43. X. Zhao, R.-C. Peng, Z. Hu, et al., "Shear-Strain-Induced Over 90° Rotation of Local Magnetization in Fecosib/Pmn-Pt (011) Multiferroic Heterostructures," *Acta Materialia* 199 (2020): 495–503.

44. H. Ahmad, J. Atulasimha, and S. Bandyopadhyay, "Reversible Strain-Induced Magnetization Switching in Fega Nanomagnets: Pathway to a Rewritable, Non-Volatile, Non-Toggle, Extremely Low Energy Straintronic Memory," *Scientific Reports* 5, no. 1 (2015): 18264.

45. G. Pradhan, F. Celegato, A. Magni, et al., "Electric Field Control of Magnetization Reversal in Fega/Pmn-Pt Thin Films," *Journal of Physics: Materials* 7, no. 1 (2024): 015016.

46. T. H. Lahtinen, K. J. Franke, and S. van Dijken, "Electric-Field Control of Magnetic Domain Wall Motion and Local Magnetization Reversal," *Scientific Reports* 2, no. 1 (2012): 1–6.

47. C.-Y. Liang, S. M. Keller, A. E. Sepulveda, et al., "Electrical Control of a Single Magnetoelastic Domain Structure on a Clamped Piezoelectric Thin Film–Analysis," *Journal of Applied Physics* 116, no. 12 (2014).

48. I. Fina, A. Quintana, X. Martí, et al., "Reversible and Magnetically Unassisted Voltage-Driven Switching of Magnetization in Ferh/Pmn-Pt," *Applied Physics Letters* 113, no. 15 (2018): 152901.

49. P. Li, Y. Zhao, S. Zhang, et al., "Spatially Resolved Ferroelectric Domain-Switching-Controlled Magnetism in Co40fe40b20/Pb (mg1/3nb2/3) 0.7 ti0. 3o3 Multiferroic Heterostructure," *ACS Applied Materials & Interfaces* 9, no. 3 (2017): 2642–2649.

50. Y. Ba, Y. Liu, P. Li, et al., "Spatially Resolved Electric-Field Manipulation of Magnetism for Cofeb Mesoscopic Discs on Ferroelectrics," *Advanced Functional Materials* 28, no. 11 (2018): 1706448.

51. T. Wu, P. Zhao, M. Bao, et al., "Domain Engineered Switchable Strain States in Ferroelectric (011)[Pb ($Mg_{1/3}$ nb $_{2/3}$)o $_3$] $_{(1-x)}$ -[PbTiO $_3$] $_x$ (PMN-PT, x ≈0.32) Single Crystals," *Journal of Applied Physics* 109, no. 12 (2011): 124101.

52. B. Noheda, D. Cox, G. Shirane, J. Gao, and Z.-G. Ye, "Phase Diagram of the Ferroelectric Relaxor (1- x) Pbmg 1/3 nb 2/3 o 3- x Pbtio 3," *Physical Review B* 66, no. 5 (2002): 054104.

53. T. Wu, A. Bur, P. Zhao, et al., "Giant Electric-Field-Induced Reversible and Permanent Magnetization Reorientation on Magnetoelectric ni/(011)[Pb (Mg1/3nb2/3) o3](1- x)–[Pbtio3] X Heterostructure," *Applied Physics Letters* 98, no. 1 (2011).

54. M. Buzzi, R. V. Chopdekar, J. L. Hockel, et al., "Single Domain Spin Manipulation by Electric Fields in Strain Coupled Artificial Multiferroic Nanostructures," *Physical review letters* 111, no. 2 (2013): 027204.

55. J. Atulasimha and A. B. Flatau, "A Review of Magnetostrictive Iron–Gallium Alloys," *Smart Materials and Structures* 20, no. 4 (2011): 043001.

56. G. Pradhan, F. Celegato, G. Barrera, et al., "Magnetic Properties of Fega/Kapton for Flexible Electronics," *Scientific Reports* 12, no. 1 (2022): 17503.

57. G. Barrera, D. Martella, F. Celegato, et al., "Light-Controlled Magnetic Properties: An Energy-Efficient Opto-Mechanical Control Over Magnetic Films by Liquid Crystalline Networks," *Advanced Science* 11, no. 47 (2024): 2408273.

58. P. Meisenheimer, R. Steinhardt, S. Sung, et al., "Engineering New Limits to Magnetostriction through Metastability in Iron-Gallium Alloys," *Nature Communications* 12, no. 1 (2021): 2757.

59. D. Damjanovic, "Ferroelectric, Dielectric and Piezoelectric Properties of Ferroelectric Thin Films and Ceramics," *Reports on progress in physics* 61, no. 9 (1998): 1267.

60. M. Hinterstein, K.-Y. Lee, S. Esslinger, et al., "Determining Fundamental Properties from Diffraction: Electric Field Induced Strain and Piezoelectric Coefficient," *Physical Review B* 99, no. 17 (2019): 174107.

61. M. Goiriena, Z. Xiao, R. Steinhardt, et al., "Imaging of Voltage-Controlled Switching of Magnetization in Highly Magnetostrictive Epitaxial Fe–Ga Microstructures," *Nanoscale* 16, no. 18 (2024): 9021–9028.

62. E. Zhao, Z. Fang, M. Cheng, et al., "In Situ Observation of Two-Step 90° Domain Reversal with Different Characteristics in Pmn–38% Pt Single Crystal," *Journal of Materials Science* 55 (2020): 8041–8049.

63. G. Vinai, F. Motti, V. Bonanni, et al., "Reversible Modification of Ferromagnetism through Electrically Controlled Morphology," *Advanced Electronic Materials* 5, no. 7 (2019): 1900150.

64. D. Dagur, A. M. Finardi, V. Polewczyk, et al., "Thermal Treatment Effects on Pmn-0.4 pt/fe Multiferroic Heterostructures," *ACS Applied Electronic Materials* 6, no. 9 (2024): 6648–6656.

65. G. Vinai, F. Motti, A. Y. Petrov, et al., "An Integrated Ultra-High Vacuum Apparatus for Growth and In Situ Characterization of Complex Materials," *Review of Scientific Instruments* 91, no. 8 (2020).

66. G. Panaccione, I. Vobornik, J. Fujii, et al., "Advanced Photoelectric Effect Experiment Beamline at Elettra: A Surface Science Laboratory Coupled with Synchrotron Radiation," *Review of Scientific Instruments* 80, no. 4 (2009).

Supporting Information

Additional supporting information can be found online in the Supporting Information section.

Supporting Information